Mapping Microvasculature with Acoustic Angiography Yields Quantifiable Differences between Healthy and Tumor-bearing Tissue Volumes in a Rodent Model[1]

Ryan C. Gessner, BS
Stephen R. Aylward, PhD
Paul A. Dayton, PhD

Purpose: To determine if the morphologies of microvessels could be extracted from contrast material–enhanced acoustic angiographic ultrasonographic (US) images and used as a quantitative basis for distinguishing healthy from diseased tissue.

Materials and Methods: All studies were institutional animal care and use committee approved. Three-dimensional contrast-enhanced acoustic angiographic images were acquired in both healthy ($n = 7$) and tumor-bearing ($n = 10$) rats. High-spatial-resolution and high signal-to-noise acquisition was enabled by using a prototype dual-frequency US transducer (transmit at 4 MHz, receive at 30 MHz). A segmentation algorithm was utilized to extract microvessel structure from image data, and the distance metric (DM) and the sum of angles metric (SOAM), designed to distinguish different types of tortuosity, were applied to image data. The vessel populations extracted from tumor-bearing tissue volumes were compared against vessels extracted from tissue volumes in the same anatomic location within healthy control animals by using the two-sided Student t test.

Results: Metrics of microvascular tortuosity were significantly higher in the tumor population. The average DM of the tumor population (1.34 ± 0.40 [standard deviation]) was 23.76% higher than that of the control population (1.08 ± 0.08) ($P < .0001$), while the average SOAM (22.53 ± 7.82) was 50.73% higher than that of the control population (14.95 ± 4.83) ($P < .0001$). The DM and SOAM metrics for the control and tumor populations were significantly different when all vessels were pooled between the two animal populations. In addition, each animal in the tumor population had significantly different DM and SOAM metrics relative to the control population ($P < .05$ for all; P value ranges for DM, 3.89×10^{-7} to 5.63×10^{-3}; and those for SOAM, 2.42×10^{-12} to 1.57×10^{-3}).

Conclusion: Vascular network quantification by using high-spatial-resolution acoustic angiographic images is feasible. Data suggest that the angiogenic processes associated with tumor development in the models studied result in higher instances of vessel tortuosity near the tumor site.

[1] From the Joint Department of Biomedical Engineering, University of North Carolina, Chapel Hill and North Carolina State University, 304 Taylor Hall, 109 Mason Farm Rd, Chapel Hill, NC 27599-6136 (R.C.G., P.A.D.); and Department of Medical Imaging, Kitware, Carrboro, NC (S.R.A.).
Received October 3, 2011; revision requested December 2; revision received February 2, 2012; accepted February 17; final version accepted March 22. R.C.G. supported by the National Science Foundation's Graduate Research Fellowship Program. P.A.D. supported by pilot funding from the University of North Carolina Lineberger Cancer Center.
Address correspondence to P.A.D. (e-mail: *padayton@bme.unc.edu*).

Ultrasonography (US) is an attractive medical imaging modality because of its relatively low cost, portability, and low level of invasiveness. Microbubble contrast agents in conjunction with specialized acoustic pulsing and receiving schemes have enabled the detection of blood flow in microvessels whose backscattered acoustic signal would otherwise be obscured in noise. Microbubble contrast agents, when introduced into the blood stream, can circulate for several minutes before being cleared from the system (1).

There are several methods in preclinical and clinical settings to extract quantitative data from contrast material–enhanced US images to assess organ health and disease state. Examples of these methods include perfusion imaging (2,3) and molecular imaging (4,5). Typically, these methods attempt to monitor either the amount of blood flow within a tissue volume (by examining the increase in US signal from blood pool contrast agents) or the presence of molecular markers of disease (through imaging of targeted contrast agents retained in the tissue), respectively. While some groups have recently demonstrated the ability to quantify the morphology, or architecture, of blood vessels and blood vessel networks in thyroid and breast tumors, this approach has been limited by the resolution of the low-frequency contrast detection approaches used in these studies (6–8).

Vessel structural abnormalities are known to reveal underlying disease very early during the onset of disease (9), even after the introduction of only tens of cells to an in vivo tissue environment (10). Moreover, vessel abnormalities have been shown to resolve, or normalize, with the administration of a successful therapy (11). Thus, analyzing the morphology of a vascular network within a diseased tissue volume provides a very sensitive method to assess the effects of therapy, which is particularly necessary when clinicians are seeking to tune their personalized therapeutic approaches (12).

Demonstrated herein is a combination of an algorithm for vessel segmentation, metrics for vessel morphologic analysis (13), and a high-spatial-resolution high-contrast imaging approach, which together form a system for vascular mapping (acoustic angiography). Similar vessel segmentation and analysis methods have been previously implemented for tissue disease and tumor response assessment in magnetic resonance (MR) angiographic data (9,11,14,15). The physics of dual-frequency contrast-enhanced imaging, which enables the acoustic angiographic approach essential to microvessel segmentation, have been previously described by Kruse and Ferrara (16), and the design of the prototype imaging transducer has been previously presented by Gessner et al (17). The purpose of this analysis was to test our hypothesis that the morphologies of microvessels could be extracted from US images and used as a quantitative basis for distinguishing healthy from diseased tissue volumes in a rat model.

Advances in Knowledge

- A new US approach, acoustic angiography, enables high-spatial-resolution noninvasive microvascular mapping.
- A segmentation algorithm can be used to extract microvessel morphology from acoustic angiographic images.
- A quantitative analysis of microvessel morphologies illustrates significant differences in tortuosity metrics between healthy and tumor tissue; average increase in tortuosity in the tumor-bearing population over the healthy population was 23.76% and 50.73%, depending on the metric ($P < .0001$).

Implications for Patient Care

- The combination of acoustic angiography with a quantitative microvascular analysis technique can noninvasively provide information about the presence of microvascular tortuosity abnormalities associated with tumor presence and growth.
- This result suggests that US, which is low cost, safe, and portable, can be used to depict the downstream vascular changes associated with disease onset while tumors are still very small, as well as assess tumor response to antivascular therapies.

Materials and Methods

Animal and Contrast Agent Preparation

All animal protocols used in this prospective study were approved by our institutional animal care and use committee. Animals used in this prospective study were female Fischer 344 rats (approximately 250 g, Charles River Laboratories, Durham, NC). A fibrosarcoma tumor model was established through the implantation of a 1-mm^3 sample of tissue in the right flank region of the animals as previously described (18). Animals were imaged after the tumor had grown larger than 0.5 cm in each of the three principal axes. The right flanks of control ($n = 7$) and tumor-bearing ($n = 10$) animals were imaged. Prior to imaging, the area around the right flank

Published online before print
10.1148/radiol.12112000 **Content codes:** VA US

Radiology 2012; 264:733–740

Abbreviations:
DM = distance metric
SOAM = sum of angles metric

Author contributions:
Guarantor of integrity of entire study, R.C.G.; study concepts/study design or data acquisition or data analysis/interpretation, all authors; manuscript drafting or manuscript revision for important intellectual content, all authors; manuscript final version approval, all authors; literature research, all authors; experimental studies, R.C.G., S.R.A.; statistical analysis, R.C.G.; and manuscript editing, R.C.G., P.A.D.

Funding:
This research was supported by the National Institutes of Health (grants R01-CA138419 and R01-EB009066).

Potential conflicts of interest are listed at the end of this article.

was shaved with an electronic clipper. A depilating cream was also applied to remove the remaining hair in the area. A 24-gauge catheter was placed in the tail vein for the administration of contrast material.

Lipid-encapsulated microbubble contrast agents were prepared as previously described (19), resulting in a polydisperse size distribution of contrast agents with a mean diameter of 0.9 μm and concentration of 1×10^{10} bubbles per milliliter. Prior to intravenous administration, microbubbles were diluted in saline to a concentration of 3.3×10^9 bubbles per milliliter. Contrast agent was continuously infused through a syringe pump (Harvard Apparatus, Holliston, Mass) at a rate of 70 μL/min.

Image Acquisition

All images were acquired, processed, and analyzed by a PhD graduate student (R.C.G., with more than 3 years of experience working with high-spatial-resolution preclinical US images). Volumetric US images were acquired with a prototype probe described in Gessner et al (17). Briefly, the probe is a modification of a commonly used high-frequency preclinical transducer (RMV 707; VisualSonics, Toronto, Ontario, Canada) with a 4-MHz element added confocally outside of the inner 30-MHz element. This configuration allows low-frequency excitation of microbubble contrast agents near resonance, promoting better contrast sensitivity and penetration depth than 30-MHz transmit-receive imaging. Furthermore, high-frequency harmonics produced by the microbubbles are received by the high-frequency element and limited only by one-way attenuation, providing substantially better resolution than would otherwise be achievable at 4-MHz transmit-receive imaging. Moreover, the difference between pulsing and receiving frequencies enables the suppression of tissue signal, because echoes from tissue contain substantially less high-frequency harmonic content than those of microbubbles. The pulsing pressure for all images was 1.23 MPa (mechanical index = 0.62), with a 15-MHz high-pass filter used on the received lines of data to further suppress tissue signal.

Images were acquired with a frame rate of 3 Hz, with a five-frame averaging step at each location to suppress spurious signal from contrast agent flowing in vessels smaller than the spatial resolution of the system. Imaging began less than 1 minute after the initiation of contrast material infusion, and each three-dimensional acoustic angiographic image required approximately 5 minutes to acquire. All three-dimensional images were acquired with an interimage elevational step size of 0.2 mm by using the linear motion stage of the US system. Control tissue volumes in this study were defined as the three-dimensional images acquired in non–tumor-bearing animals, against which the images acquired in tumor-bearing animals were compared. The tissue imaged in the control animals was the right flank, which was the same location imaged in the tumor-bearing population. Both B-mode and acoustic angiographic images were acquired, enabling retrospective vascular-tissue overlays and the delineation of tumor boundaries.

Offline Image Analysis

All image data were exported from the US system as uncompressed audio-video interleave files. The images were upsampled in the elevational direction by using a custom trilinear interpolation script written in Matlab (MathWorks, Natick, Mass) to yield isotropic voxels with a width, length, and height of 0.05 mm. This interpolation helped expedite the vessel segmentation algorithm. Microvessels were extracted from each animal's image data by using the previously described vessel segmentation algorithm based on multiscale extraction of centerlines (20). Previously described vessel morphologic metrics (13) were then applied. These metrics, which provide a means to assess two distinct types of centerline tortuosity, were the distance metric (DM) and sum of angles metric (SOAM). The DM is a measure of how far a curve meanders between its end points and is computed as the ratio of the length of the extracted vessel path and the length of the secant line between the vessel's start and end. A vessel's end points are determined by one of several criteria during the automated extraction of the vessel's centerline by the algorithm (ie, the arrival at a bifurcation). For an overview of the mechanics of the vessel extraction algorithm, the reader is referred to Aylward and Bullitt (20). The SOAM is an index of vessel tortuosity that is computed by integrating the angular changes occurring between successive pairs of points along the vessel's centerline, normalized by the total vessel path length. Occasionally, a vessel would exhibit an extremely high tortuosity value, several standard deviations away from the mean for the animal from which it was extracted. These values may have been true estimates or may have been artifacts from the imaging or analysis method. To prevent these outliers from grossly skewing the distribution of vessel tortuosities, we excluded from further analysis any vessel with either a DM or SOAM value greater than 3 standard deviations from the mean for the animal from which it was extracted. As a result of this step, between zero and two vessels were removed from each of the 17 animals in the study, with an average of 1.06 vessels ± 0.66 (standard deviation) being removed per animal. This corresponds to an average of less than 4% (number of vessels removed from an animal divided by total vessels originally extracted from that animal) of the total vessels being removed as outliers from each animal (maximum of two vessels, minimum of zero vessels). Additional information about the statistics of vascular morphologies can be found in Bullitt et al (21).

Statistical Analysis

Four types of variability in vessel tortuosity were assessed: interpopulation, intrapopulation, interanimal, and intra-animal. These types of vessel tortuosity variability are defined as follows. Interpopulation variability is the differences in vessel tortuosity occurring between group types (ie, pooled tumor-bearing animals vs pooled control animals).

Intrapopulation variability is the differences in vessel tortuosities occurring within a single population (a single tumor-bearing animal vs the pooled tumor-bearing population). This is computed by taking the standard deviation of the average tortuosity values for each animal in the population. Interanimal variability is the differences in vessel tortuosity occurring between a single animal and one or more other animals of a different animal population (a control animal vs the pooled tumor population). Finally, intraanimal variability is the range in tortuosity values reported within a single animal (a large range suggests a more heterogeneous vascular network). The mean intraanimal variability is the average intraanimal variability across all animals in the population. The relative intraanimal variability is expressed as a percentage and is computed by normalizing an animal's original intraanimal variability (ie, standard deviation) with the mean tortuosity value, thereby enabling comparisons between the variability of two different tortuosity metrics.

The statistical significance of the differences between the ensembles of microvessel segmentations of the two animal populations was assessed by using a two-tailed Student *t* test. Ensembles are defined as a collection of DM or SOAM values; they can consist of these tortuosity metrics computed on either the vessels extracted from a single animal or the pool of all vessels from the animals in a population. When animals were compared with their own group, equal variances were assumed for the *t* test; although when animals were compared with the opposite group, unequal variances were assumed. Three statistical comparisons were made between individual animals and their respective populations, as well as between the two animal populations themselves. The first comparison was used to test interpopulation variability in vessel tortuosity. All vessel segmentations were pooled into two groups, and the reported tortuosity metrics were compared to assess gross differences between the healthy and tumor-bearing populations. For this first comparison, a total of two tests were performed: the DM and SOAM ensembles from the tumor-bearing group versus the control group. The second comparison was implemented to test interanimal variability in vessel tortuosity. The ensemble of tortuosity values reported for the vessels extracted from each tumor-bearing animal was compared against the pooled control population to allow us to retrospectively simulate a "diagnosis" of these animals (ie, an individual patient's image data compared with a healthy control population's data set). Similarly, the ensemble of tortuosity values reported for the vessels extracted from each control animal was also compared against the vessels of the pooled tumor population. For this second comparison, a total of 34 tests were performed: the DM and SOAM ensembles for each of the 17 animals compared against the opposite animal group's pool. Finally, a third statistical test was used to assess intrapopulation variability in vessel tortuosity. The ensemble of tortuosity values reported for the vessels extracted from each animal in the study was compared with the pooled aggregate of their respective population (with their own data removed from the pool) to assess the consistency of the tortuosity of vessels found within each of our two populations. For this third comparison, a total of 34 tests were performed: the DM and SOAM ensembles for each of the 17 animals compared against their own animal group's pool. All three of these statistical tests were performed by using Matlab. For the first assessment, which tested the differences in vessel tortuosity between the vessels extracted from the two populations, statistical significance difference was set at *P* less than .05. In the second and third statistical assessments in which multiple comparisons were made, a Bonferroni correction was implemented and statistical significance difference was set at *P* less than .00147 (original significance level .05 divided by the 34 tests).

Results

A total of 438 microvessels were extracted and analyzed (Fig 1). The average number of vessels extracted from the image data of control flanks was 51.51% lower (15.86 vessels ± 2.41; range, 13–19 vessels) than that of the tumor models (32.7 vessels ± 9.08; range, 20–50 vessels). The average size of the 10 tumors imaged in this study was 11.4 mm ± 3.6 (range, 5.8–16.8 mm) for the longest axis, corresponding to a volume of 0.452 cm^3 ± 0.331 (range, 0.070–1.076 cm^3). Examples of segmented centerlines taken from acoustic angiographic image data can be seen in Figure 2. The average DM for the tumor population was 23.76% higher (1.34 ± 0.40) than that for the control population (1.08 ± 0.08) ($P <$ .0001) (Fig 3). The average SOAM was 50.73% higher in the tumor population relative to the control population (22.53 ± 7.82 compared with 14.95 ± 4.83) ($P <$ .0001). The intraanimal variation for the DM was 0.07 and 0.33 (control vs tumor), which corresponds to a relative deviation of 6.60% and 24.90%, respectively. For the SOAM, the average intraanimal variation was 4.82 and 7.79 (control vs tumor), which corresponds to a relative deviation of 32.10% and 34.53%, respectively (Table 1).

The difference between the pooled DM ensemble for the tumor-bearing population (1.34 ± 0.40) and the control population (1.08 ± 0.08) was significant ($P <$ .0001) (Fig 3). Similarly, the difference between the pooled SOAM ensemble for the tumor-bearing population (22.53 ± 7.82) and the control population (14.95 ± 4.83) was significant ($P <$ .0001).

The ensemble of tortuosity values computed from the vessels extracted from each tumor-bearing animal was compared against the pooled control population. The *P* value range for the 20 tests was 2.42×10^{-12} to 5.63×10^{-3}. Of the 20 tumor animal versus control group comparisons made, 18 had *P* values less than the Bonferroni-corrected *P* value of .00147. Similarly, the ensemble of tortuosity values computed from the vessels extracted from each control animal was compared against the pooled tumor-bearing population. The *P* value range for the 14 control animal versus tumor group tests was 1.11×10^{-16} to 2.09×10^{-3}. Of the 14 tests, 13 had *P* values less than the Bonferroni-corrected *P* value of .00147.

Figure 1

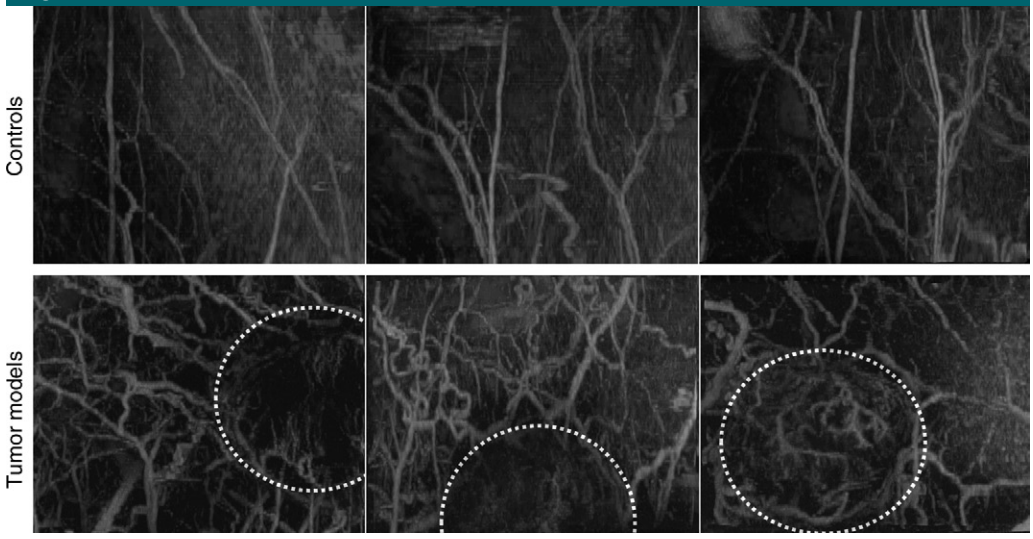

Figure 1: Maximum intensity projections through three-dimensional acoustic angiographic image data for six animals. Because these six three-dimensional data sets were projected along the axis of sound propagation, the resulting two-dimensional images are oriented in the coronal anatomic plane. The field of view for these images is 2.5 cm in the horizontal (lateral) direction and approximately 2 cm in the vertical (elevational) direction. Morphologic differences are apparent between the animal types both within and outside tumor margins. Dashed lines = approximate tumor boundaries.

Figure 2

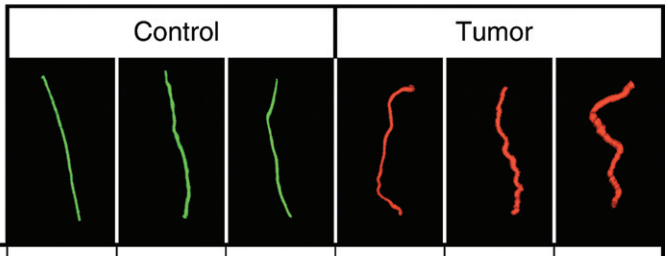

DM	1.03	1.06	1.05	1.34	1.30	1.30
SOAM	6.59	14.64	7.57	19.07	29.74	20.85

Figure 2: Six extracted vessels show how different morphologic features influence the quantitative tortuosity metrics. A slowly meandering vessel will have a higher DM, and a vessel with high-frequency oscillations will have a higher SOAM.

A summary of the *P* values for these tests is listed in Table 2.

Finally, tortuosity ensembles for each of the animals were compared against the pooled vessel ensemble for their respective group to assess intragroup heterogeneity. Thirty-four comparisons were made: one for each of the two tortuosity metrics in all 17 animals in the study. (These tests can be visualized by comparing the distributions in Figure 3, *A* and *C*, with the animal's own population pool in Figure 3, *B* and *D*.) While some of these comparisons resulted in *P* values less than .05, none had *P* values less than the Bonferroni-corrected *P* value of .00147. This suggests that while marked differences between control and tumor-bearing animal groups were apparent (as per the first and second statistical assessments), the groups were fairly consistent relative to themselves. Despite their lack of significance below the Bonferroni-corrected *P* value, there were two animals in the tumor animal versus tumor group comparisons with *P* values less than .05 compared with only one animal in the control animal versus control population comparisons with *P* values less than .05 (Table 2). This trend could suggest that the degree of intragroup vessel morphologic heterogeneity was slightly greater in the tissue volumes containing a highly angiogenic tumor.

Discussion

In this study, we presented a high-spatial-resolution minimally invasive imaging approach and a quantitative analysis of microvessel structure extracted from these three-dimensional acoustic angiographic images. All tumor-bearing animals had significant increases in both of the reported tortuosity metrics (DM and SOAM) compared with those of the vessels in the control population. The results from this study indicated we can use microvessel centerlines extracted from high-spatial-resolution acoustic angiographic images to provide a

quantitative basis for distinguishing healthy from diseased tissue volumes. The fact that animals within both control and tumor-bearing populations had significant differences from the aggregate pool of their respective groups suggests that heterogeneity is present within the microvasculature of these rodents, although our results also demonstrated there is a greater degree of vascular heterogeneity in the presence of cancer.

There were several limitations of this study. First, the prototype acoustic angiographic transducer enables excellent visualization of microvasculature but only within a narrow depth of field (< 1 cm) centered around the acoustic focus (located approximately 1.3 cm into tissue). This means that vasculature beneath tumors is rarely captured on our images unless the tumors are very small, nor are entire tumors visualized if their diameters in the axial direction exceed 1 cm. Further developments in transducer and US system technology would need to be achieved before acoustic angiography could be implemented clinically with widespread utility. Performance of this technique is currently in a similar realm of resolution and penetration depth as offered by photoacoustic imaging (22). While photoacoustic imaging does not necessitate a contrast agent to interrogate the microvasculature—an advantage over our acoustic angiography approach—to our knowledge, there are not yet systems demonstrated in the literature with simultaneous resolution and depth of penetration as utilized here. Typically, photoacoustic systems can achieve either similar spatial resolution at shallower depth of penetration (23) or similar depth of penetration at a lower resolution (24). Moreover, these systems do not possess the portability offered by acoustic angiography, and they necessitate computationally intensive reconstruction algorithms to achieve volumetric imaging.

Another limitation of the study was tumor size heterogeneity. While the tumors imaged in this study were all at least 0.5 cm in diameter, they were not all the same size and thus not at the same point in the progression of the tumor model. Because tumor volume was not standardized across the tumor-bearing animal population, the degree to which the heterogeneity between subjects (tumor volumes, percentage of necrosis, growth rates, etc) affected the interanimal deviations in the reported DM and SOAM values is unknown. In addition, the relationship between tissue perfusion speed and vessel tortuosity remains to be studied with our acoustic angiographic imaging technique; however, this is of substantial interest because a previous human MR study demonstrated that these two techniques (vessel morphologic analysis and perfusion analysis) provide independently useful diagnostic information in the assessment of brain tumors

Figure 3

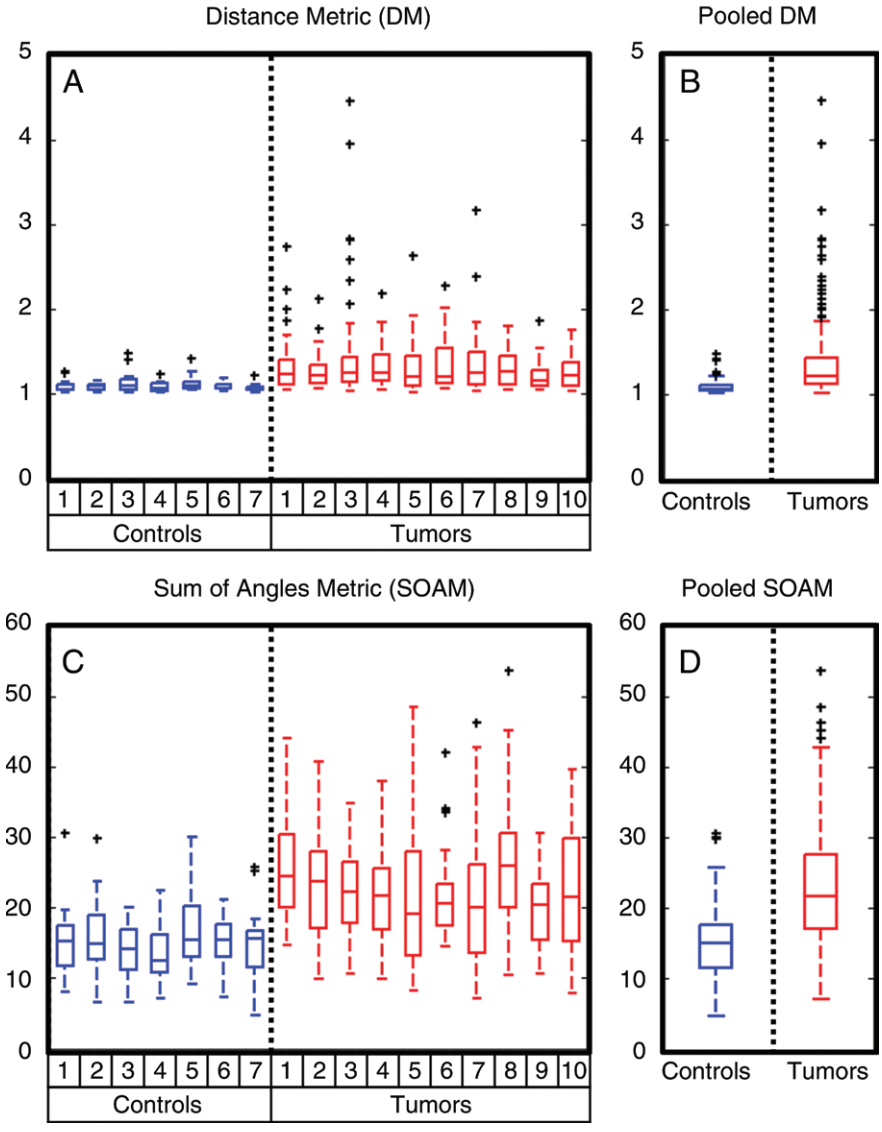

Figure 3: Box plots show the ensembles of the reported DM and SOAM values for the vessels extracted from the right flanks of the two different animal populations—healthy *(Controls)* and tumor-bearing *(Tumors)* animals. *A, C,* The ensemble of each animal in the study. *B, D,* The pooled ensemble for the control and tumor-bearing groups.

Table 1

Summary of the Two Tortuosity Metrics for Control and Tumor-bearing Animal Populations

	DM		SOAM	
Parameter	Control Population	Tumor Population	Control Population	Tumor Population
Maximum	1.47	4.45	30.48	53.67
Minimum	1.01	1.01	4.64	7.05
Mean	1.08	1.34	14.95	22.53
Intrapopulation variability	0.08	0.40	4.83	7.82
Intraanimal variability	0.07	0.33	4.82	7.79
Relative intraanimal variability (%)	6.60	24.90	32.10	34.53

Note.—Computations for these quantities are found in the text.

Table 2

Summary of *P* Values for the Statistical Tests Used to Assess Interanimal and Intrapopulation Variability in Vessel Tortuosity

	DM		SOAM	
Group and Animal	Pooled Control Population	Pooled Tumors	Pooled Control Population	Pooled Tumors
Control animals				
1	.62	<.000147*†	.75	<.000147*†
2	.66	<.000147*†	.47	.0010*
3	.025	<.000147*†	.41	<.000147*†
4	.63	<.000147*†	.19	<.000147*†
5	.09	<.000147*†	.18	.002
6	.61	<.000147*†	.95	<.000147*†
7	.09	<.000147*†	.99	<.000147*†
Tumor-bearing animals				
1	<.000147*†	.89	<.000147*†	.007
2	.0002*	.41	<.000147*†	.79
3	.0002*	.004	<.000147*†	.79
4	<.000147*†	.91	<.000147*†	.47
5	.0006*	.76	.0016	.28
6	<.000147*†	.94	<.000147*†	.85
7	.0005*	.81	.0004*	.38
8	.0006*	.78	.0002*	.046
9	.0056	.16	.0014*	.11
10	<.000147*†	.14	<.000147*†	.86

Note.—Each cell indicates a comparison between the ensemble of vessel tortuosities for the animal in each row and the pooled population in each column.

* *P* values are less than the Bonferroni-corrected *P* value of .00147.

† *P* values more than 10 times smaller than the Bonferroni-corrected *P* value of .00147.

(15). Finally, the syngeneic tumor grafts utilized here likely will have different microvascular development characteristics than spontaneous tumors. Hence, although we have demonstrated the utility of the imaging and analysis techniques described here, the trends between tumor-bearing and healthy tissue may translate differently to human conditions.

Future studies using this quantitative morphologic analysis of vessel structure will test the relationship between vessel tortuosity and other ultrasonic methods for assessing disease state in genetically engineered animal models to compare their relative sensitivities and uniqueness of diagnostic information. In addition, the temporal sensitivity of the technique will also be evaluated, because vascular tortuosity abnormalities have been observed when fewer than 100 cancer cells are present (10); thus, techniques capable of resolving microvasculature are exciting candidate strategies for early cancer detection and rapid assessments of response to therapy.

Practical applications: An ideal bedside clinical imaging modality is one which can sensitively, accurately, safely, and inexpensively predict therapeutic response, particularly in an era when medicine is becoming increasingly personalized. Thus, the capability of advanced US imaging and analysis techniques may have a substantial role in the future of cancer diagnostics and assessment. We predict that the technique for detecting the presence of cancer demonstrated in this article, with further development, could be used for rapid bedside disease assessment in several clinical settings.

Acknowledgments: The authors thank F. Stuart Foster, PhD, and his team, including Marc Lukacs, PhD, Mike Lee, and Emmanuel Cherin, PhD, for their collaborative efforts in fabrication of the dual-frequency US transducer prototype utilized to acquire data presented in this article. The authors also appreciate the assistance of Mark Dewhirst, DVM, PhD, for generously providing the fibrosarcoma tissue samples used to establish our tumor model, James Tsuruta, PhD, for the fabrication of all contrast agents used in this study, Brandon Frederick, BS, for providing the custom image interpolation script, and biostatistician Allison Deal, MS, for her contributions to the statistical analyses.

Disclosures of Potential Conflicts of Interest: R.C.G. No potential conflicts of interest to disclose. **S.R.A.** Financial activities related to the present article: none to disclose. Financial activities not related to the present article: author employed by Kitware, which provides software consulting services for a multitude of companies in the medical field; grants have been proposed and funded on this topic (from Kitware); University of North Carolina has filed a patent on some of the technologies discussed. Other relationships: none to disclose. **P.A.D.** Financial activities related to

the present article: none to disclose. Financial activities not related to the present article: author is a consultant for and is on the Scientific Advisory Board of Targeson (no money received, but PI has stock options); institution receives grants from American Heart Association, Focused Ultrasound Foundation, and Department of Defense; author receives payment for lectures from Jefferson Ultrasound Institute; author receives payment for manuscript preparation from the *Journal of Molecular Imaging* (2010); patent disclosure has been filed that is relevant to some of the technology in the article, patent has been licensed and no funds have been received. Other relationships: none to disclose.

References

1. Lindner JR. Microbubbles in medical imaging: current applications and future directions. Nat Rev Drug Discov 2004;3(6):527–532.
2. Wilson SR, Burns PN. Microbubble-enhanced US in body imaging: what role? Radiology 2010;257(1):24–39.
3. Carr CL, Lindner JR. Myocardial perfusion imaging with contrast echocardiography. Curr Cardiol Rep 2008;10(3):233–239.
4. Gessner R, Dayton PA. Advances in molecular imaging with ultrasound. Mol Imaging 2010;9(3):117–127.
5. Lindner JR. Molecular imaging of cardiovascular disease with contrast-enhanced ultrasonography. Nat Rev Cardiol 2009;6(7):475–481.
6. Molinari F, Mantovani A, Deandrea M, Limone P, Garberoglio R, Suri JS. Characterization of single thyroid nodules by contrast-enhanced 3-D ultrasound. Ultrasound Med Biol 2010;36(10):1616–1625.
7. Huang SF, Chang RF, Moon WK, Lee YH, Chen DR, Suri JS. Analysis of tumor vascularity using three-dimensional power Doppler ultrasound images. IEEE Trans Med Imaging 2008;27(3):320–330.
8. Eisenbrey JR, Joshi N, Dave JK, Forsberg F. Assessing algorithms for defining vascular architecture in subharmonic images of breast lesions. Phys Med Biol 2011;56(4):919–930.
9. Bullitt E, Lin NU, Ewend MG, et al. Tumor therapeutic response and vessel tortuosity: preliminary report in metastatic breast cancer. Med Image Comput Comput Assist Interv 2006;9(pt 2):561–568.
10. Li CY, Shan S, Huang Q, et al. Initial stages of tumor cell-induced angiogenesis: evaluation via skin window chambers in rodent models. J Natl Cancer Inst 2000;92(2):143–147.
11. Bullitt E, Ewend M, Vredenburgh J, et al. Computerized assessment of vessel morphological changes during treatment of glioblastoma multiforme: report of a case imaged serially by MRA over four years. Neuroimage 2009;47(suppl 2):T143–T151.
12. Kamen BA, Glod J, Cole PD. Metronomic therapy from a pharmacologist's view. J Pediatr Hematol Oncol 2006;28(6):325–327.
13. Bullitt E, Gerig G, Pizer SM, Lin W, Aylward SR. Measuring tortuosity of the intracerebral vasculature from MRA images. IEEE Trans Med Imaging 2003;22(9):1163–1171.
14. Bullitt E, Zeng D, Gerig G, et al. Vessel tortuosity and brain tumor malignancy: a blinded study. Acad Radiol 2005;12(10):1232–1240.
15. Parikh AH, Smith JK, Ewend MG, Bullitt E. Correlation of MR perfusion imaging and vessel tortuosity parameters in assessment of intracranial neoplasms. Technol Cancer Res Treat 2004;3(6):585–590.
16. Kruse DE, Ferrara KW. A new imaging strategy using wideband transient response of ultrasound contrast agents. IEEE Trans Ultrason Ferroelectr Freq Control 2005;52(8):1320–1329.
17. Gessner R, Lukacs M, Lee M, Cherin E, Foster FS, Dayton PA. High-resolution, high-contrast ultrasound imaging using a prototype dual-frequency transducer: in vitro and in vivo studies. IEEE Trans Ultrason Ferroelectr Freq Control 2010;57(8):1772–1781.
18. Streeter JE, Gessner R, Miles I, Dayton PA. Improving sensitivity in ultrasound molecular imaging by tailoring contrast agent size distribution: in vivo studies. Mol Imaging 2010;9(2):87–95.
19. Feingold S, Gessner R, Guracar IM, Dayton PA. Quantitative volumetric perfusion mapping of the microvasculature using contrast ultrasound. Invest Radiol 2010;45(10):669–674.
20. Aylward SR, Bullitt E. Initialization, noise, singularities, and scale in height ridge traversal for tubular object centerline extraction. IEEE Trans Med Imaging 2002;21(2):61–75.
21. Bullitt E, Muller KE, Jung I, Lin W, Aylward S. Analyzing attributes of vessel populations. Med Image Anal 2005;9(1):39–49.
22. Hu S, Wang LV. Photoacoustic imaging and characterization of the microvasculature. J Biomed Opt 2010;15(1):011101.
23. Zhang EZ, Laufer JG, Pedley RB, Beard PC. In vivo high-resolution 3D photoacoustic imaging of superficial vascular anatomy. Phys Med Biol 2009;54(4):1035–1046.
24. Song KH, Wang LV. Deep reflection-mode photoacoustic imaging of biological tissue. J Biomed Opt 2007;12(6):060503.